

Geo-spatial Information Science



ISSN: 1009-5020 (Print) 1993-5153 (Online) Journal homepage: www.tandfonline.com/journals/tgsi20

The interannual variations of installed capacity for offshore wind turbines in China: estimations derived solely from remote sensing

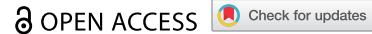
Qiannan Ding, Chunpeng Chen, Bo Tian, Wenxiang Ji, Bin Zhang, Xue Li & Qing Yuan

To cite this article: Qiannan Ding, Chunpeng Chen, Bo Tian, Wenxiang Ji, Bin Zhang, Xue Li & Qing Yuan (30 Apr 2025): The interannual variations of installed capacity for offshore wind turbines in China: estimations derived solely from remote sensing, Geo-spatial Information Science, DOI: 10.1080/10095020.2025.2496393

To link to this article: https://doi.org/10.1080/10095020.2025.2496393

9	© 2025 Wuhan University. Published by Informa UK Limited, trading as Taylor & Francis Group.
+	View supplementary material 🗹
	Published online: 30 Apr 2025.
	Submit your article to this journal 🗷
hh	Article views: 433
Q	View related articles 🗹
CrossMark	View Crossmark data ☑







The interannual variations of installed capacity for offshore wind turbines in China: estimations derived solely from remote sensing

Qiannan Ding (Da), Chunpeng Chen (Da), Bo Tian (Da), Wenxiang Ji (Da), Bin Zhang (Da), Xue Li (Da) and Qing Yuan 102

^aState Key Laboratory of Estuarine and Coastal Research, East China Normal University, Shanghai, China; ^bJC STEM Lab of Earth Observations, Department of Land Surveying and Geo-Informatics, The Hong Kong Polytechnic University, Hong Kong, China; 'Research Centre for Artificial Intelligence in Geomatics, The Hong Kong Polytechnic University, Hong Kong, China

ABSTRACT

Accurately and thoroughly determining the installed capacity of offshore wind turbines (OWTs) and offshore wind farms (OWFs) is crucial for evaluating offshore wind energy and guiding future development. However, existing statistical data only provide aggregated information on capacity, and detailed attribute data are not publicly available for free. Here, we present a novel pure remote sensing method to estimate the OWT installed capacity, successfully applied to estimate the installed capacity of OWTs in China from 2015 to 2022. This approach first used deep learning to identify turbine shadows from Sentinel-2 images, then estimated the hub height corresponding to the shadows by combining the solar elevation angle, and finally related the height to the capacity through a polynomial model. The results demonstrate that the pure remote sensing method exhibits excellent performance in estimating the installed capacity of OWTs. Comparing the generated single OWT capacity with the officially published results, the root mean square error (RMSE) is 0.27 MW (5.06%). From the end of 2015 to 2022, the total installed capacity of OWTs in China's mainland increased from 1.06 GW to 30.18 GW, with the highest annual growth rate reaching 149.92%. These remote sensing-based estimates closely match the data documented in the existing reports ($R^2 = 0.99$, RMSE = 0.62 GW). The average capacity per turbine increased from 4 MW to 4.84 MW, and the maximum capacity of OWFs increased from 632.89 MW in 2015 to 1305.04 MW in 2022 (geographically). By the end of 2022, OWFs with an installed capacity exceeding 100 MW accounted for 90.83% of the total number of OWFs in China's mainland, indicating a trend toward larger-scale development of OWFs. This study provides a reference for large-scale assessments of OWT installed capacity. Additionally, it can be used for the construction of high-capacity OWFs to design future installations.

ARTICLE HISTORY

Received 2 August 2024 Accepted 17 April 2025

KEYWORDS

Offshore wind turbines; Sentinel-2; deep learning; installed capacity; renewable energy

1. Introduction

With the intensification of global climate issues over the past few decades, offshore wind energy has emerged as a popular clean energy source due to its high storage capacity, zero pollution, and technical maturity (Duan 2017; Feng et al. 2015; Wass 2018). In recent years, the construction of offshore wind turbines (OWTs) has expanded significantly worldwide, emerging as a major application of wind energy. Between 2016 and 2020, global OWTs surged from 4,642 units to 9,441 units, reflecting a remarkable growth rate of 103.38% (Hoeser, Feuerstein, and Kuenzer 2022). In 2022, new offshore wind installations globally reached 8.8 GW, bringing the total installations to 64.3 GW (Global Wind Energy Council 2023). China's recent and total installations were 5 GW and 31.4 GW, respectively, both ranking first globally. Moreover, the formulation of the 14th Five-Year Plan and the "dual carbon" goals indicate

that the future development of offshore wind power equipment in China will continue to increase. Estimating the installation of OWTs is of great significance for national efforts to combat climate change, transition to renewable energy, facilitate project financing in the offshore wind power industry, and enhance public awareness (Du et al. 2024). Consequently, the China Wind Energy Association (CWEA) and the Global Wind Energy Council (GWEC) have publicly provided annual summary information on the national-scale installed capacity of OWTs. The data sources are primarily derived from market intelligence, project lists, and data submitted by companies. These data, therefore, need to be verified through multiple channels, making the process timeconsuming, labor-intensive, and costly.

Remote sensing technology offers significant opportunities for monitoring large-scale offshore targets and can serve as an alternative to field surveys

(Fan et al. 2024; Gong et al. 2025; Greidanus et al. 2017; Liang et al. 2025). Several researchers have utilized remote sensing imagery to explore the spatial distribution of OWTs, providing a basis for inferring installed capacity. Xu et al. (2020) employed optical satellite images and visual saliency detection algorithms to detect the geographical distribution of OWTs. Moubayed, Becker, and Blankenbach (2025), Wang et al. (2024), Zhang et al. (2021) leveraged the strong backscatter characteristics of OWTs in Sentinel-1 synthetic aperture radar (SAR) imagery, combined with threshold analysis and morphological extraction, to determine the spatial locations of OWTs. However, determining the spatial location and number of OWTs alone is insufficient to estimate the installed capacity of an offshore wind farm (OWF). and Kuenzer (2022)demonstrated a monotonic relationship between the installed capacity of an OWT and the hub height of the turbine, which provides an opportunity to estimate the installed capacity of an OWF through remote sensing. However, as Majidi Nezhad et al. (2022) pointed out, the siting of OWTs must consider their environmental impact, which is often directly related to their type. Despite this, large-scale, high-precision data on OWT installed capacity and corresponding hub height remain scarce. Additionally, previous research has consistently pointed out that obtaining accurate hub height measurements for offshore wind turbines remains a technical difficulty (Badger et al. 2016; Medina-Lopez et al. 2021; Wang, Ullrich, and Millstein 2018).

Building on these insights, significant challenges remain in deriving the hub height of OWTs from remote sensing to estimate installed capacity. The first major difficulty is accurately estimating hub height from remote sensing data. Currently, several methods exist for extracting object height data using multi-source remote sensing data. The first method is light detection and ranging (LiDAR), which can directly obtain high-precision three-dimensional point cloud measurements of object heights (Gong et al. 2011; Wang et al. 2024). However, collecting continuous and large-scale information on the heights of OWTs is difficult due to the high cost of acquiring point cloud data (Liu et al. 2023). The second method involves radar technologies, such as single/stereo SAR, interferometric SAR, and spotlight SAR (Magruder, Neuenschwander, and Klotz 2021; Sun et al. 2022; Zhu and Bamler 2010). However, radar images are affected by signals mixed with different microwave scattering mechanisms, and the specular reflection effect of waterbodies significantly reduces radar backscatter intensity, resulting in relatively high uncertainty in height extraction (Lee and Hong 2024; Sun et al. 2019). The third method uses stereo images from aerial or drone imagery (Pepe et al. 2021; Wang et al.

2021). This method requires high-quality image stereo matching and faces challenges of feasibility and continuity in areas where drones cannot reach or where stereo pairs are lacking (Cao and Huang 2021; Frantz et al. 2021).

The abovementioned methodologies employ direct measurements to ascertain the heights of wind turbines. However, estimating wind turbine heights is inherently uncertain and unstable due to the challenges associated with image acquisition and suboptimal image quality in the sea environment. Consequently, these methods do not suit hub height estimation in large-scale sea surface environments. Indirect estimation of object heights using the shadows of objects in sunlight, combined with satellite imaging angles, is a commonly used method in remote sensing (Huang et al. 2022). However, determining shadow thresholds necessitates manual intervention, which reduces the accuracy and efficiency of shadow extraction in large volumes of remote sensing data (Hu and Zhang 2018; Huang and Zhang 2012). In addition, OWT hub shadows have fewer effective pixels and share similar spectral information to waterbodies and dark-colored objects in remote sensing images. Therefore, traditional methods that calculate hub height using shadow thresholds are challenging to implement on a large scale (Sun et al. 2019). The second difficulty is effectively modeling the relationship between hub height and installed capacity. For this aim, a sufficient number of known OWT hub heights and corresponding installed capacity data are required. However, collecting these data is time-consuming and restricted by policies and regulations in some countries.

The Sentinel-2 satellite, developed under the European Space Agency (ESA), provides highresolution (10 m) multi-temporal satellite imagery, which has been widely used for offshore target recognition, including wind turbines, ships, oil and gas extraction platforms, and marine pollutants (Beaumont et al. 2019; Ciocarlan and Stoian 2021; Kikaki et al. 2024; Mandroux et al. 2021). Sentinel-2 is also frequently used for object shadow identification to estimate object height (Frantz et al. 2021; Moubayed, Becker, and Blankenbach 2025), making it a potential data source for OWT hub shadow recognition. Moreover, with the development of deep learnimage segmentation ing-based convolutional neural networks (CNNs) have been used to segment typical elements in highly heterogeneous coastal environments (Bai et al. 2023; Han et al. 2025; Zhang et al. 2024). For example, Chen et al. (2023b) used the U-Net model integrating a dual attention mechanism and edge supervision to accurately segment tidal flats in highly turbid and tidally dynamic offshore environments. Similarly, Aghdami-Nia et al. (2022) accurately extracted coastlines from remote sensing images of the Chinese coast and the southern Caspian Sea by modifying the standard U-Net model and developing an automatic coastline extraction framework. Hence, open-source highresolution remote sensing imagery and deep learning models present an opportunity for accurately extracting OWT hub shadows, facilitating the calculation of OWT hub heights and the assessment of installed capacity. However, the proportion of wind turbine shadow pixels is minimal compared to the vast sea surface, and it remains uncertain whether deep learning models can effectively handle feature recognition and segmentation in this context.

Given the aforementioned issues, this study developed a Sentinel-2 imagery and deep learning-based shadow extraction method for OWTs, aiming to overcome the reliance of traditional methods on manual intervention and high-quality imagery. It achieves large-scale estimation of installed wind turbine capacity solely based on Sentinel-2 remote sensing data for the first time. This approach provides a new perspective for clean energy monitoring through remote sensing technologies. Additionally, it offers scientific support for achieving China's "dual carbon" goals and optimizing offshore wind power development policies. The specific objectives of this study are as follows: (1) To develop a deep learning-based shadow extraction method for OWTs to accurately calculate wind turbine hub heights; (2) To construct a relationship model between turbine hub height and installed capacity; (3) To evaluate the change in China's installed offshore wind capacity from 2015 to 2022 using remote sensing.

2. Study area

The study area encompasses 12 coastal provinciallevel administrative regions in China's mainland. A single-sided buffer zone extending 150 km from the coastline is established, with the boundary of this buffer zone defined as the study area (Figure 1(a)). The 150 km setting considers the current maximum offshore distance of OWTs in China and the spatial locations of OWTs under construction. The offshore wind energy potential at depths of 5-50 m and a height of 70 m is estimated to be approximately 500 GW (Yi 2018). Moreover, areas above 70 m in height, situated in deeper and more distant seas, hold even greater potential for technological development. Currently, there are 11 international databases and 24

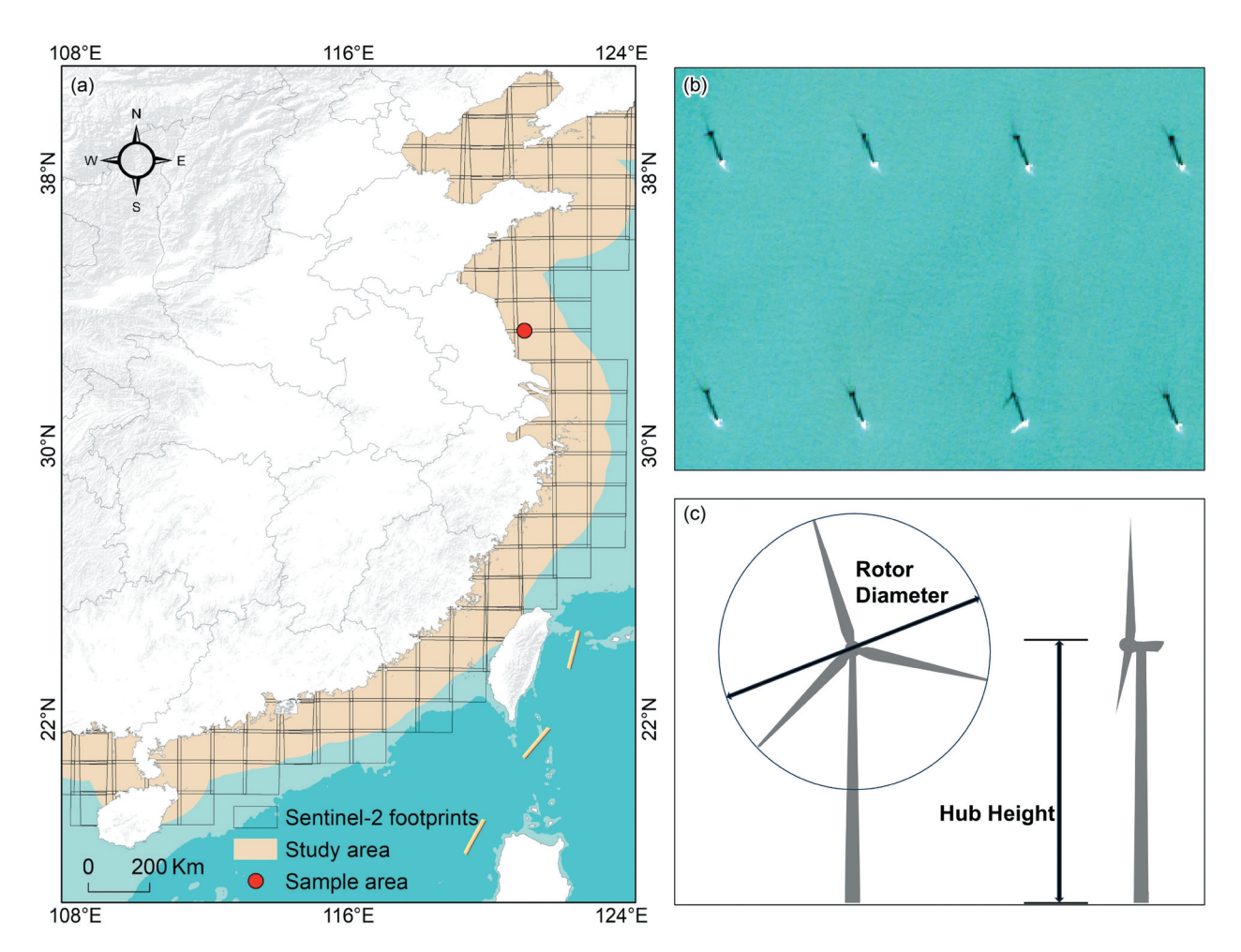


Figure 1. (a) The study area and its corresponding sentinel-2 footprints; (b) sentinel-2 image of Jiangsu on 19 December 2022, displayed in false color with bands b8, b4, and b3; (c) schematic diagram of an OWT.

regional/national databases containing statistical data on OWTs and OWFs (Pazheri, Othman, and Malik 2014). While some databases provide detailed information, they require payment (e.g. 4C Offshore), while others lack temporal consistency and global coverage (e.g. USWTD, Rand et al. 2020) and GBWSFs (Dunnett et al. 2020). According to the GOWT dataset (Zhang et al. 2021), as of December 2019, there are 1,853 offshore wind units in China, primarily located off the coasts of Jiangsu and Fujian. In this study, the spatial location data for OWTs from 2015 to 2022 are derived from the code accompanying the GOWT dataset (Zhang et al. 2021), selected for its open accessibility, methodological generalization over time, and accurate geospatial information, which can be applied on the Google Earth Engine (GEE) platform.

3. Data and methods

3.1. Data collection

We downloaded the multispectral Sentinel-2 Level 2A atmospheric correction surface reflectance images from the GEE platform and utilized the QA60 band mask cloud pixels. The CLOUDY_ PIXEL_PERCENTAGE attribute was set to 60% to ensure image quality without significantly reducing the number of available images (Chen et al. 2023a). Given that small OWT shadows at higher solar elevation angle (SEA) can lead to inaccurate and lowprecision shadow extraction, we limited the image date range to within ± 15 days of December 22 each year from 2015 to 2022. This 30-day interval allows for complete spatial coverage of the study areas. Consequently, a total of 5,944 images were used: 435 in 2015, 396 in 2016, 805 in 2017, 603 in 2018, 991 in 2019, 857 in 2020, 892 in 2021, and 965 in 2022. We defined the geographical boundaries of the OWT locations. Then, we examined the cloud cover to ascertain whether the turbines were visible in each image. Images where the turbines were obscured by clouds were omitted from our analysis. Subsequently, we selected a single Sentinel-2 image closest to December 22 for each year from 2015 to 2022 within the study area and downloaded them using strip number. For each downloaded Sentinel-2 image, we recorded the satellite overpass date, longitude, latitude, and SEA based on the available image attributes.

To validate the accuracy of our findings, we gathered information on the models, hub heights, and installed capacities of OWTs from 80 OWFs in China. Data was sourced from platforms, such as 4C Offshore, The Wind Power, and Wind-turbine-models. This dataset encompasses many regions including Liaoning, Hebei, Tianjin, Shandong, Jiangsu, Shanghai, Zhejiang, Fujian, and Guangdong.

Additionally, it involves multiple OWT manufacturers, such as Goldwind, Siemens, MingYang, Envision Energy, Sinovel, and CSIC Haizhuang Windpower Equipment.

3.2. Estimation of OWT installed capacity

The method for estimating installed offshore wind capacity using purely remote sensing consists of three steps: (1) Deep learning for extracting OWT hub shadows; (2) OWT Hub Height Calculation; and (3) OWT installed capacity estimation based on OWT hub shadows.

3.2.1. Deep learning for extraction of OWT hub shadows

3.2.1.1. Training dataset preparation. Deep learning requires a large number of representative samples to achieve good accuracy and generalization. In this study, we selected the Subei Shoal, an area with a high density and strong clustering of offshore wind turbines (OWTs), as the sample region. Sentinel-2 imagery of the Subei Shoal, acquired on 19 December 2023, was used for analysis. To select suitable band combinations that make the target object attributes more distinct for deep learning training, we calculated the band reflectance characteristics and the corresponding absolute differences (ABSD) for OWT shadows and background pixels in the 13 Sentinel-2 bands. Ultimately, we selected the b8, b4, and b3 bands at 10 m resolution (Table 1). These images used for training contain a total of 9 OWFs (where OWTs with the same arrangement interval and direction are considered as one OWF) and 352 OWTs. They cover various underlying surfaces, including different depths of waterbodies and tidal flats. In these images, OWT hub shadows appear as distinct black features contrasted with the blue water and brown soil. We then manually extracted the shadows of the 352 OWTs from the 9 OWFs through multi-person visual interpretation, resulting in segmentation results. The training images were further processed in ArcGIS Pro, where a sliding window approach was applied with a step size of 128 pixels. During window cropping, each slice was moved by 128 pixels, resulting in 50% overlaps between adjacent slices. This method helps the model capture image continuity and contextual information more effectively, reducing edge effects and preventing semantic information loss at the slice boundaries. These training images were cropped into a total of 960 (256 \times 256 pixels in size) deep learning sample slices (Figure 2). This sample database was randomly divided into a training set of 768 samples and a validation set of 192 samples in an 8:2 ratio to better evaluate the performance and generalization ability of the model. To further improve the model's performance and generalization ability, all training

Table 1. Comparison	of	sentinel-2	resolution	and	reflection	characteristics	in (different
bands.								

Bands	Shadow	Background	ABSD	Spatial resolution (m)
B1	0.3003	0.3005	0.0002	60
B2	0.2714	0.2746	0.0032	10
B3	0.2587	0.2644	0.0058	10
B4	0.2697	0.2796	0.0099	10
B5	0.2699	0.2797	0.0098	20
B6	0.2431	0.2517	0.0086	20
B7	0.2420	0.2510	0.0091	20
B8	0.2248	0.2341	0.0093	10
B8A	0.2127	0.2200	0.0074	20
B9	0.1328	0.1327	0.0000	60
B10	0.1013	0.1013	0.0000	60
B11	0.1120	0.1121	0.0001	20
B12	0.1076	0.1077	0.0001	20

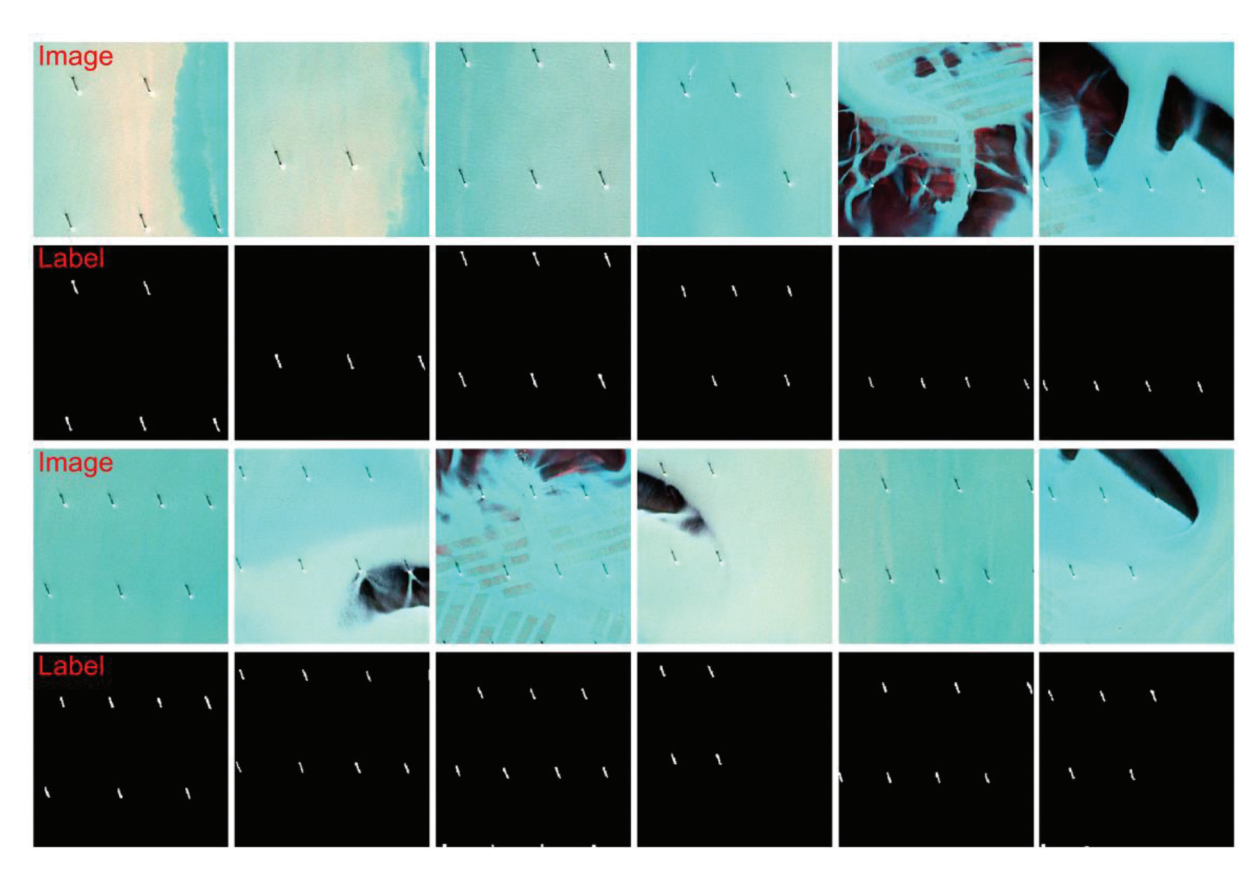


Figure 2. Examples of sentinel-2 ACE-enhanced imagery and corresponding labels in Sheyang and Dafeng, Jiangsu, with sample slice sizes of 256×256 pixels.

samples underwent random rotation (±90°) and were processed using the automatic color equalization (ACE) algorithm. The ACE algorithm locally and nonlinearly adjusts the images' brightness, color, and contrast, correcting the final pixel values by considering the dark relationships between pixels to enhance local features.

3.2.1.2. The architecture of deep learning. U-Net is a fully convolutional neural network initially proposed for image segmentation in 2015 (Ronneberger, Fischer, and Brox 2015). It features a U-shaped network structure with an encoder-decoder architecture (Figure 3(a)). The encoder captures contextual information by gradually reducing spatial dimensions and

extracting high-level features. The decoder restores resolution through upsampling and incorporates skip connections with the encoder's feature maps to retain detail. Its advantages include learning from small samples, utilizing skip connections for feature fusion, and performing multi-level feature extraction. The backbone convolutional network is critical for deep image recognition and semantic segmentation (Benali Amjoud and Amrouch 2020; He et al. 2019). Classic convolutional backbone networks have improved the accuracy of image recognition tasks, including VGG (Simonyan and Zisserman 2015), ResNet (He et al. 2016), DarkNet (Redmon and Farhadi 2017), and GoogLeNet (Szegedy et al. 2015). To enhance the performance of the classic U-Net architecture, we

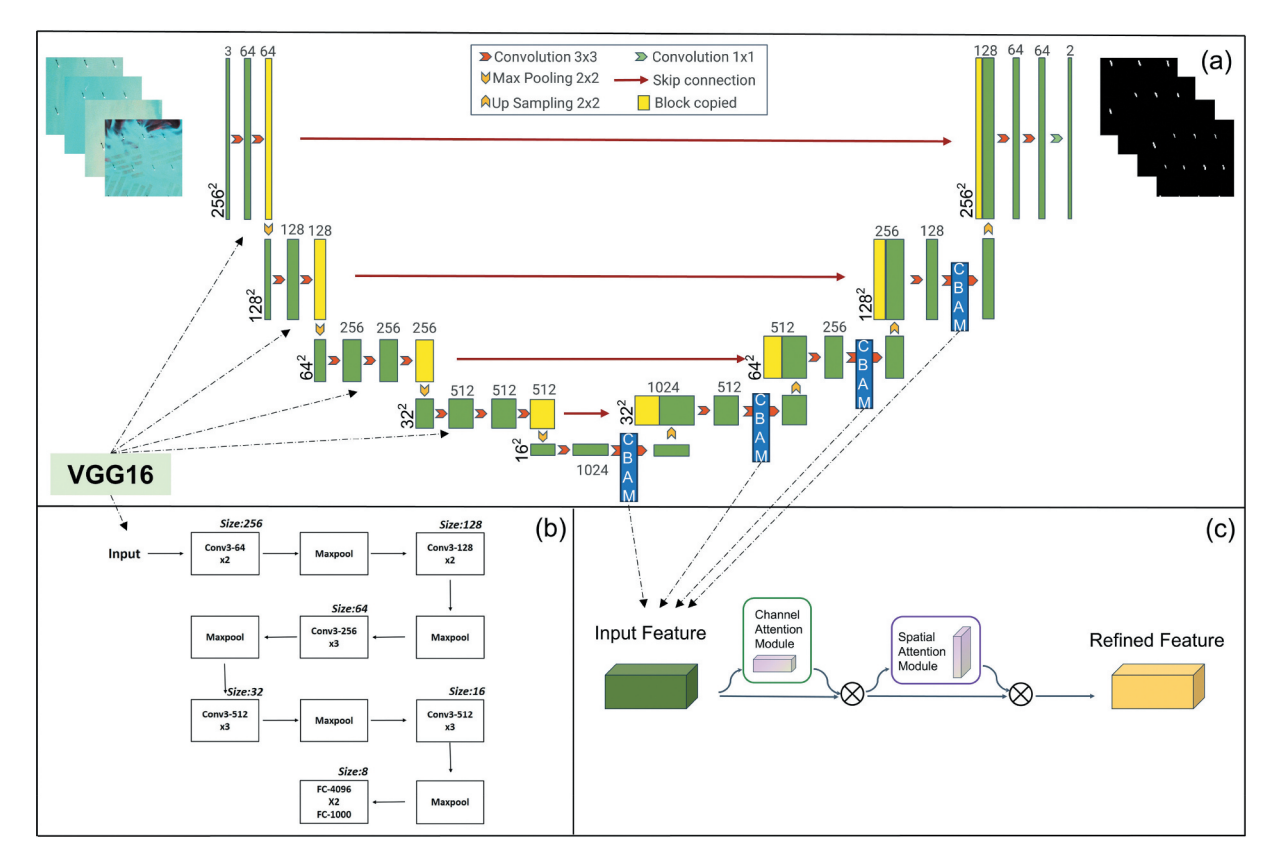


Figure 3. (a) VC-Unet model structure diagram; (b) VGG16 network architecture; (c) CBAM attention mechanism module.

made two modifications in this study: (1) integrating the first four convolutional blocks of the deep network VGG16 backbone as the encoding components of the U-Net architecture, and (2) adding a CBAM attention mechanism before each upsampling in the decoding phase to accurately segment the wind turbine shadow boundaries. The proposed deep learning model is referred to as VC-Net. The modified deep learning model is called VC-Unet.

The VGG network is one of the classic models in deep learning, widely used in computer vision tasks for semantic segmentation due to its simple structure and ease of implementation. The VGG network constructs deep neural networks using a series of small convolutional kernels (3 \times 3) and pooling layers (2×2) , which increase the receptive field without adding computational complexity, thereby providing stronger non-linear capacity. Additionally, reducing the number of parameters lowers the risk of overfitting and improves the network's feature extraction ability. The 16-layer network is known as VGG16. VGG16 has an architecture, with 13 alternating convolutional and pooling layers, followed by 3 fully connected layers for classification (Figure 3(b)). In this study, we replaced the encoder part of the U-Net network with the network structure of VGG16 before the fourth max pooling layer. Each block contains 64, 128, 256, and 512 convolutional layers. Deep learning requires a significant amount of training samples to extract features effectively. However, due to the limited Sentinel-2 imagery training data, we used transfer learning techniques to enhance feature extraction (Zhuang et al. 2020). We utilized pre-trained weights from the VGG16 backbone network, as using the initial pre-trained parameters provides more stable training results than random initialization.

The convolutional block attention module (CBAM) (Woo et al. 2018), improves the performance of CNNs by integrating channel attention and spatial attention, thereby enhancing perceptual capability without substantially increasing network complexity. By adaptively learning channel and spatial attention weights, the CBAM module captures correlations between features across different dimensions, thus improving the performance of image recognition tasks and addressing the limitations of traditional CNNs when handling information of varying scales and directions. Initially, the maximum and average feature values are calculated for each channel. The feature vectors obtained from global max pooling and average pooling are then fed into a fully connected layer, where the Sigmoid activation function is applied to derive the final channel attention weight vector. The max-pooled and average-pooled features are concatenated along the channel dimension, creating a feature map with different scale context information. The resulting feature map is subsequently processed by a convolutional layer to generate spatial attention weights. The output features from both the channel and the spatial attention modules are then multiplied element-wise to produce the final attention-enhanced features (Figure 3 (c)). This enhanced feature set serves as input for the subsequent network layers, retaining key information while suppressing noise and irrelevant data.

3.2.1.3. Model implementation and training. The VC-Unet model is implemented in Python using PyTorch. Sentinel-2 images and their corresponding labels were randomly divided into training and validation datasets in an 8:2 ratio. The training was conducted in two phases: the freezing phase and the unfreezing phase. The freezing phase requires less memory, reducing the demands on machine performance. If, after 10 epochs, there was no improvement in training accuracy or reduction in validation loss, the training process was terminated prematurely. The total number of training epochs was set to 200, with 40 epochs allocated to the freezing phase. The model was compiled using the Adam optimizer with an initial learning rate of 1e-4, and the optimizer's internal momentum parameter was set to 0.9. After every 2 epochs, the training weights were automatically saved, and the validation dataset was assessed every 5 epochs. To address the imbalance between positive and negative samples in the dataset, we used Dice Loss to mitigate the negative impact of foregroundbackground imbalance, allowing the model to focus more on the foreground regions during training. Additionally, we combined the Focal Loss function to further address the sample imbalance issue, ensuring that the model's attention is concentrated on the objects of interest.

3.2.1.4. Model evaluation metrics. To comprehensively assess the effectiveness of the backbone network and decoder for OWT hub shadow segmentation, we selected common metrics used in semantic segmentation, including accuracy, average precision (AP), mean average precision (mAP), intersection over union (IoU), and F1-Score. Accuracy measures the extent to which repeated measurements agree with the true value, evaluating the ratio of correctly predicted samples to the total number of samples. AP integrates the precisionrecall curve, representing the combined performance of precision and recall. mAP represents the weighted average of APs across various categories. IoU, on the other hand, assesses the spatial overlap between the algorithm's predictions and the true ground-truth labels. As for the F1-Score, it is a weighted harmonic mean of precision and recall, offering a holistic metric that is less susceptible to the influence of imbalanced samples. Let us delve into the specific calculation methods:

$$Accuracy = \frac{TP + TN}{TP + TN + FP + FN} \tag{1}$$

$$AP = \int_{0}^{1} P(R)dR \tag{2}$$

$$loU = \frac{TP}{TP + FP + FN} \tag{3}$$

$$F1-Score = \frac{2 \times TP}{2 \times TP + FP + FN}$$
 (4)

$$Precision = \frac{TP}{TP + FP} \tag{5}$$

$$Recall = \frac{TP}{TP + FN} \tag{6}$$

where TP, TN, FP, and FN represent the number of pixel-level True Positives (correctly predicted target pixels), True Negatives (correctly predicted background pixels), False Positives (background pixels predicted as target pixels), and False Negatives (target pixels predicted as background pixels). Additionally, higher accuracy, mAP, IoU, and F1-Score values indicate greater accuracy in OWT hub shadow segmentation.

3.2.2. OWT hub height calculation

Given the relatively large pixel size of remote sensing imagery, achieving a balance between model accuracy and processing speed is imperative. To address this concern, we implemented a series of preprocessing steps. First, each downloaded Sentinel-2 image from GEE was cropped into a sequence of 256×256 pixel tiles. Subsequently, these tiles underwent segmentation for waterbodies and OWT hub shadows using the trained VC-Unet model. Following segmentation, the predicted output tiles were amalgamated and transformed into polygon vector files representing segmented contours. To streamline the contours, we employed the Douglas-Peucker algorithm from OpenCV, fine-tuning the threshold to uphold contour accuracy while mitigating computational overhead. In practical scenarios, OWT shadows tend to exhibit approximately rectangular shapes. However, identification outcomes often manifest as irregular polygons due to the inherent characteristics of raster data. To address this discrepancy, we employed ArcGIS's Minimum Bounding Geometry tool that delineates the smallest enclosing rectangle around each shadow (see Figure 4(a)). The length of this enclosing rectangle serves as a proxy for the shadow length of the OWTs' hubs.

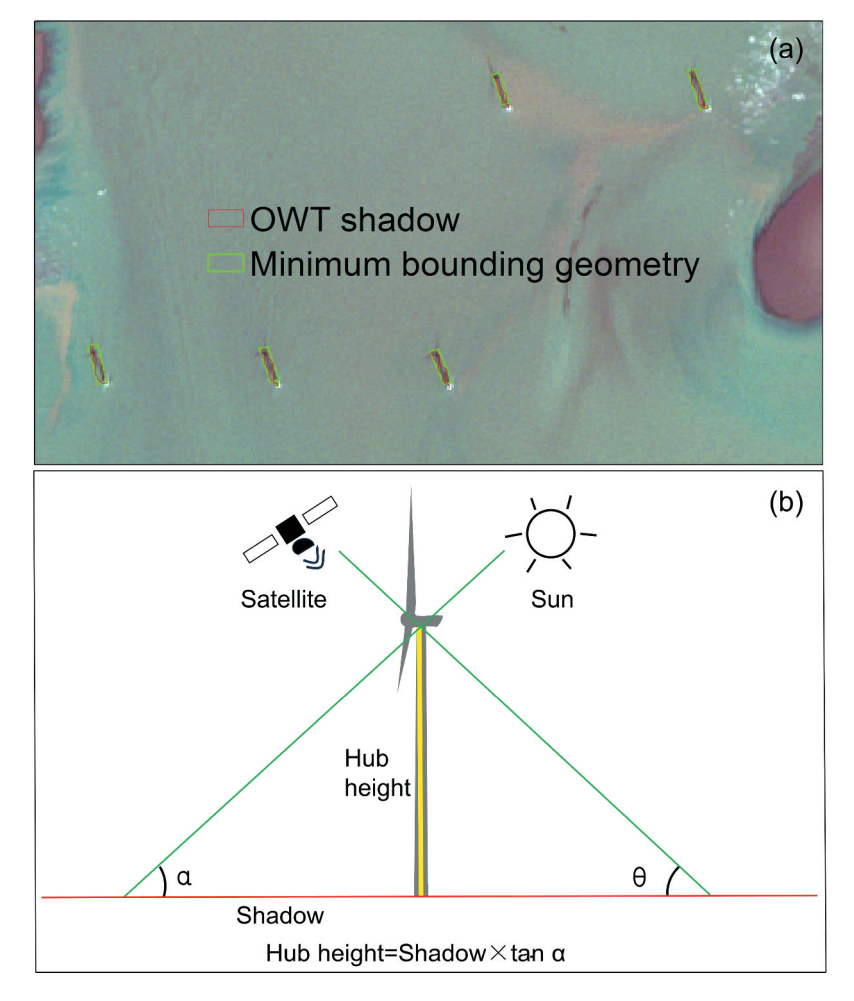


Figure 4. (a) The OWT hub shadows and minimum bounding geometry of jiangjiasha H2 300MW OWF in Rudong, Jiangsu in 2022; (b) the calculation method of OWT hub height.

Figure 4(b) illustrates the principle of calculating OWT hub heights using Sentinel-2 data and SEA. We selected Sentinel-2 data from around December 22nd of each year from 2015 to 2022, coinciding with the time when the sun is approaching the Tropic of Capricorn. Leveraging the latitude position of the OWT and the specific acquisition time of the Sentinel-2 image, we determined the SEA, denoted as α (as defined by Equation 7), where φ represents the geographical latitude, δ signifies the solar declination, and t represents the hour angle. The exact spatial locations of the OWTs were obtained using the openly accessible code associated with Zhang et al. (2021). Through the application of trigonometry and considering the length of the OWT hub shadows, we calculated the hub height of each OWT, thereby enabling the determination of the hub height for OWF within the study area. To minimize errors arising from individual turbine calculations and based on the assumption of consistent wind turbine models (hub heights) within an OWF, we selected the median hub height of all OWTs within each OWF to define the hub height for that specific OWF.

$$\sin\alpha = \sin\varphi \times \sin\delta + \sin\varphi \times \cos\delta \times \cos t \qquad (7)$$

3.2.3. OWT installed capacity estimation

We randomly selected 60 OWFs from publicly available sources and conducted a fitting analysis using the hub height and installed capacity for these 60 OWFs. In this analysis, the independent variable is the hub height of the OWTs, while the dependent variable is the installed capacity. We applied polynomial curve fitting, linear fitting, exponential fitting, and logarithmic fitting to the hub heights of OWTs ranging from 60 m to 120 m and their corresponding installed capacities using these fitting methods. The results are illustrated in Figure 5. Among the fitting methods, polynomial curve fitting yielded the highest R² value of 0.75. Therefore, we utilized polynomial curve fitting to model the installed capacity of each OWT based on the computed hub height in this study.

4. Results

4.1. Accuracy assessment

The accuracy of the VC-Unet model in extracting shadows of wind turbines from Sentinel-2 images

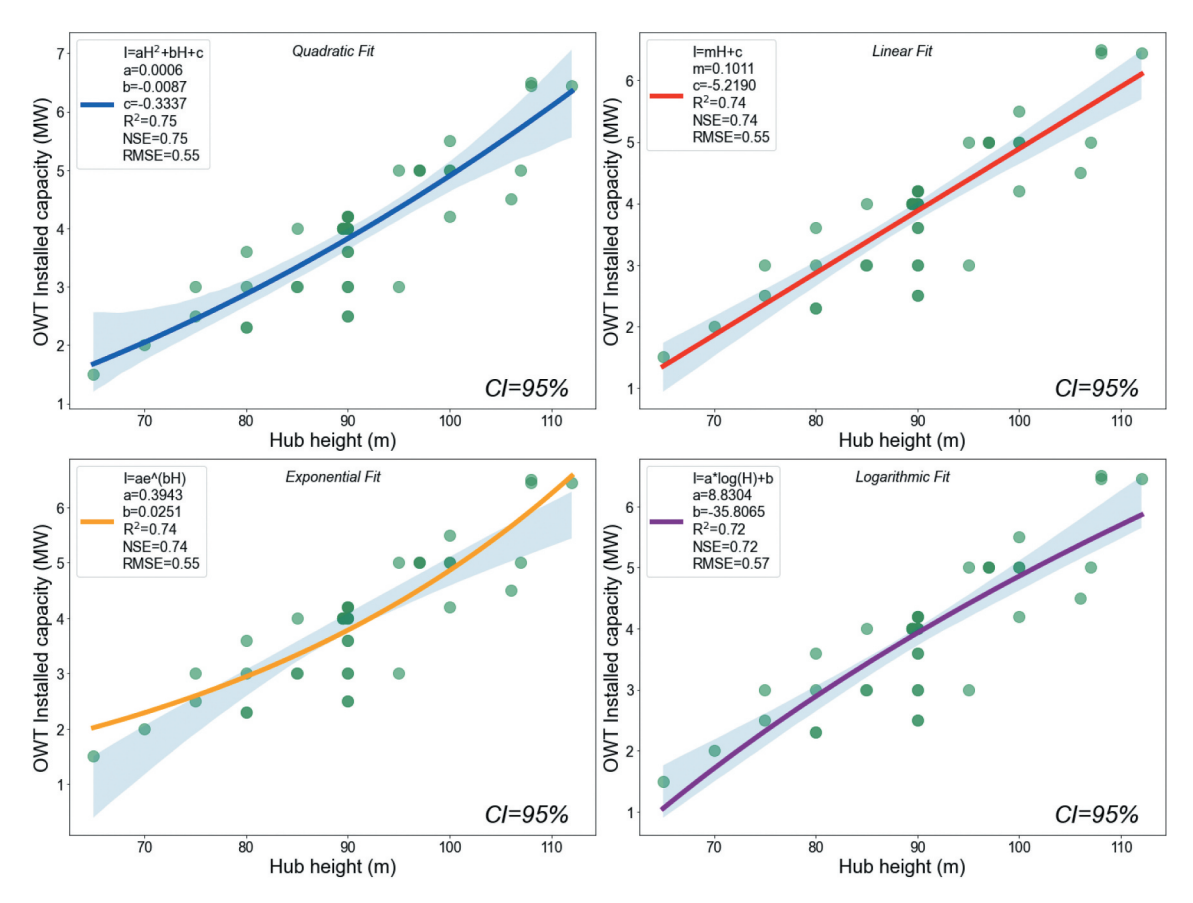


Figure 5. Hub height and installed capacity of a single OWT fitted using polynomial curve fitting, linear fitting, exponential fitting, and logarithmic fitting.

was quantitatively evaluated using a test dataset comprising 192 patches. Different random seeds were used each time, and multiple values were obtained by testing multiple times on the same dataset. The results revealed that the model achieved an IoU of 98.96 \pm 0.05, mPA of 99.66 \pm 0.03, precision of 99.58 \pm 0.01, recall of 99.38 \pm 0.06, and an F1-score of 99.48 \pm 0.02, respectively. Ablation experiments and data evaluation of the VC-Unet model are shown in Table S1. To assess the accuracy of our calculations, we compared the hub height and installed capacity of OWTs derived from Sentinel-2 observations with official ground-truth data. Specifically, we computed errors in OWT hub height and installed capacity using 20 observed OWT data points and 20 official OWT data points for comparison. Figure 6 illustrates that the variance of the calculated OWT hub height accounts for 83.79% of the variance in the official hub height, with a mean absolute error (MAE) of 1.20 m and a root mean square error (RMSE) of 1.72 m (1.74%). Considering that the spatial resolution of Sentinel-2 images is 10×10 m, there exists an inherent pixellevel theoretical error of \pm 10 m. The MAE of 1.20 m effectively demonstrates the accuracy and robustness of extracting OWT hub heights using Sentinel-2 imagery and deep learning models. In addition, the variance of the single-unit installed capacity derived from Sentinel-2 data is 101.83% of the official installed capacity variance, with a MAE of 0.19 MW and an RMSE of 0.27 MW (5.06%). The MAE of 0.19 MW indicates the accuracy and reliability of the model, while the RMSE of 0.27 MW reflects a high degree of consistency between the observed results and the actual values. This consistency provides a solid foundation for the stable prediction of OWT installed capacity and future OWF project planning.

4.2. Installed capacity of OWTs

4.2.1. Installed capacity of OWTs in 2022

Using the VC-Unet model and subsequent processing, we computed the hub height distribution for OWTs in China's mainland for the year 2022, as depicted in Figure 7. We employed the median hub height of OWTs to represent the hub height of each OWF, considering OWTs with similar geographical patterns, spacings, and orientations as part of the same OWF. The results indicate that the average hub height for OWTs in China's mainland is 99.02 m. Zhejiang boasts the highest average hub height at 105.42 m, while Fujian has the lowest at 93.47 m. For OWTs in water depths ≤25 m, the average hub height is 98.79 m, while for those in water depths >25 m, the average hub height is 102.66 m. Additionally, we computed the maximum and minimum hub heights for OWFs in



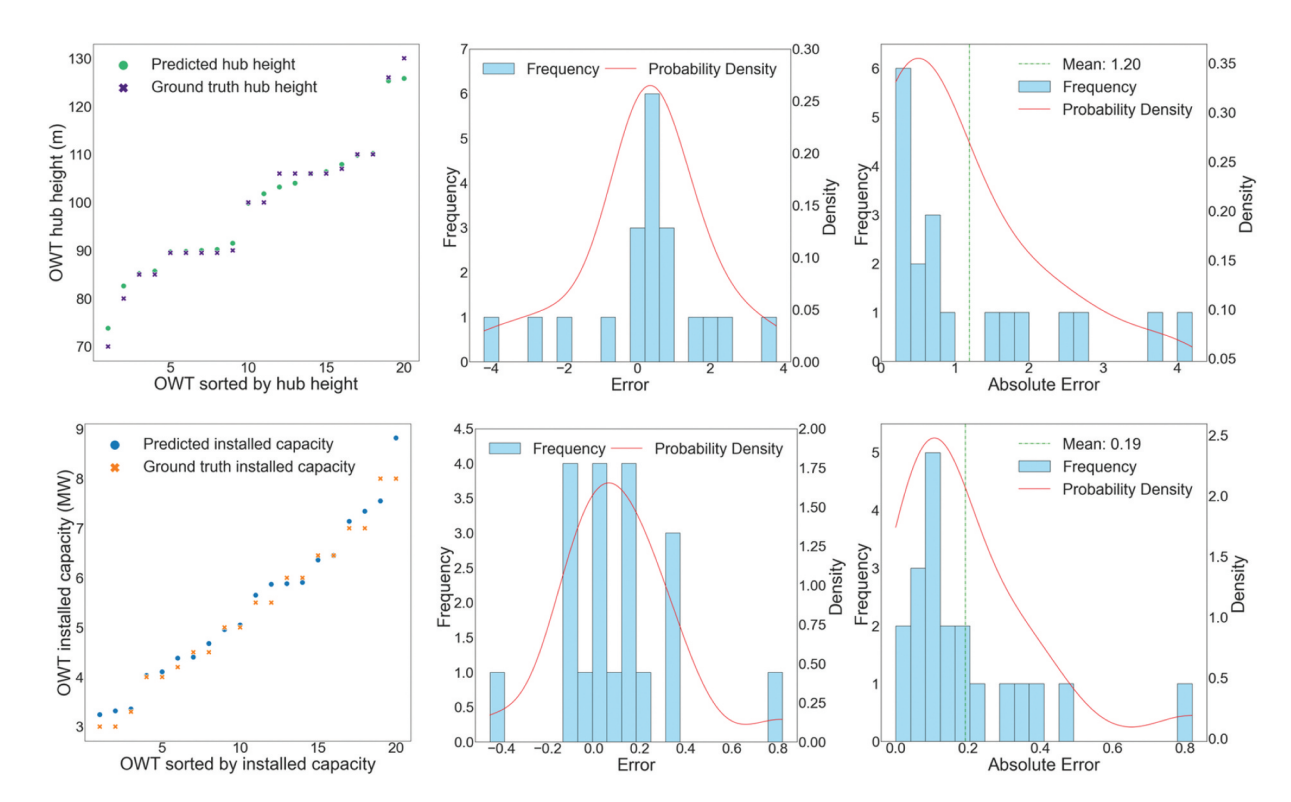


Figure 6. Error analysis of calculated OWT hub height and installed capacity. The first row presents the error and absolute error analysis for the predicted OWT hub height compared with the official data. The second row illustrates the error and absolute error analysis for the predicted installed capacity compared with the official OWT installed capacity data.

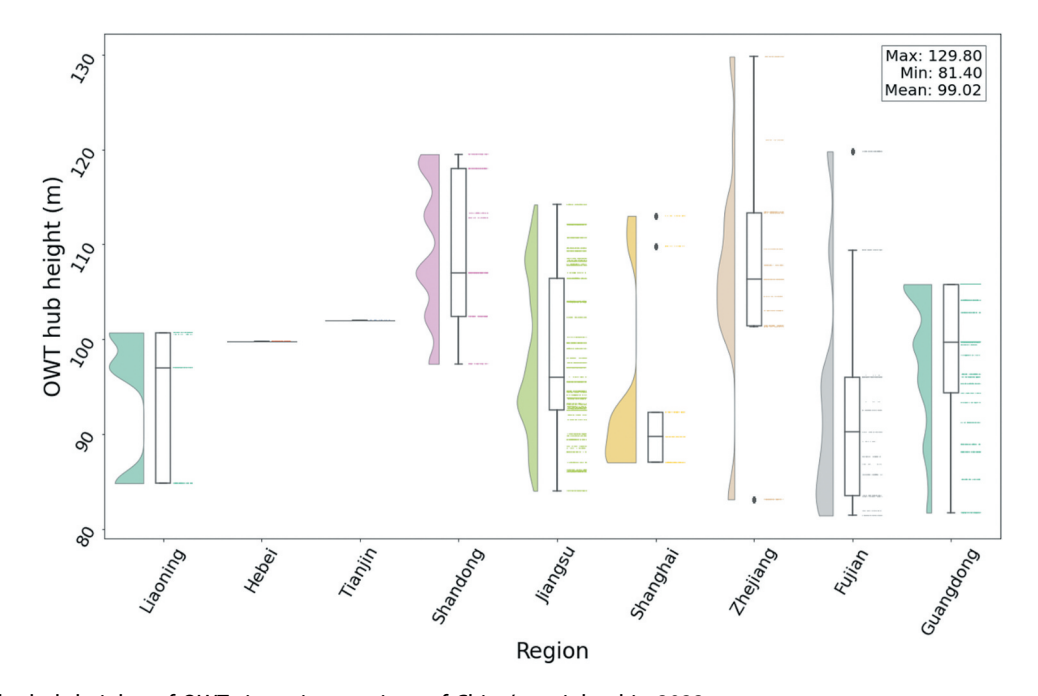


Figure 7. The hub heights of OWTs in various regions of China's mainland in 2022.

various regions. The maximum hub height is in Zhejiang at 129.8 m, while the minimum is in Fujian at 81.4 m. OWT hub heights ranging from 90 to 110 m have become the market mainstream, accounting for 89.17% of the total number of OWTs in 2022.

Based on the fitting between hub height and installed capacity, a polynomial model with a high coefficient of determination was selected as the capacity estimation model for the study area. Analyzing the relationship

between the hub height and installed capacity of OWTs, along with considering factors such as quantity, solar altitude angle, and latitude in 2022, enables a more accurate estimation of the installed capacity for each OWF. As of December 2022, 6,198 OWTs were distributed across 109 OWFs geographically, with a cumulative installed capacity of 30.18 GW. Regionally, Jiangsu leads in OWT development with a total installed capacity of 13.73 GW, accounting for 45.45% of the national total.

Other significant contributors are Guangdong (6.30 GW), Zhejiang (3.08 GW), Shandong (2.65 GW), Fujian (2.36 GW), Liaoning (0.90 GW), Shanghai (0.72 GW), Hebei (0.38 GW), and Tianjin (0.09 GW). Coastal provinces are vigorously advancing wind energy development, with substantial installed capacities of OWTs evident in southern regions, while northern areas remain in nascent development stages, offering considerable growth opportunities.

Table 2 displays the number of OWTs in each province, along with the maximum, minimum, and average installed capacities for each OWF. The average installed capacities of OWTs across different regions range from 4.27 MW to 6.05 MW, while the national average installed capacity of OWTs is 4.84 MW. Figure 8 illustrates the installed capacities of OWFs in each province and the corresponding average hub height. The most expansive OWF boasts an installed capacity of 1,305.04 MW. Among the 109 OWFs, 99 possess installed capacities exceeding 100 MW, constituting 90.83% of the total, while 41 OWFs exceed 300 MW, representing 68.33% of the total.

4.2.2. Annual dynamics of installed capacity of **OWTs**

We calculated the distribution of hub heights of OWTs in China's mainland from 2015 to 2022 (Figure 9). The results indicate an overall increasing trend in the average hub height of OWFs in China's mainland, from 90.6 m in 2016 to 99.02 m in 2022, with a growth rate of 9.3%. The decrease in the average hub height from 2015 to 2016 was primarily due to the establishment of an OWF in the northern part of Nanri Island, Fujian Province, in 2016, with an OWT hub height of 81.4 m, which was lower than the minimum OWT height of 84 m observed in Chao Bay, Jiangsu Province, in 2015. We also analyzed the variation in the maximum hub height of OWFs from 2015 to 2022. The maximum hub height exhibited a yearly increasing trend, from 96 m in 2015 to 129.8 m in 2022, with a growth rate of 35.2%. Additionally, detailed information on the maximum, minimum, and average hub heights of each province from 2015 to 2022 is provided in the supplementary material (Figure S1).

This study further estimated the single-unit installed capacity of OWTs and the installed capacity of OWFs from 2015 to 2022. Table 3 illustrates the trends from 2015 to 2022 in the number of OWTs and OWFs examined in this study, detailing the maximum, minimum, and average installed capacity per unit. In addition, it indicates the annual cumulative installed capacity. Overall, both the number of OWTs and cumulative installed capacity in China's mainland have continued to increase, demonstrating significant progress in

Table 2. Minimum, maximum, average, and total values of OWT count and installed capacity

by region in 2022.					
Region	Count	Min	Max	Mean	Total (GW)
Liaoning	208	3.32	4.98	4.34	0.90
Hebei	77	4.88	4.88	4.88	0.38
Tianjin	18	5.13	5.13	5.13	0.09
Shandong	443	4.61	7.34	6.05	2.65
Jiangsu	2900	3.24	6.63	4.73	13.70
Shanghai	168	3.53	6.48	4.26	0.91
Zhejiang	536	3.16	8.82	5.74	2.88
Fujian	552	3.00	7.38	4.27	2.36
Guangdong	1296	3.03	5.58	4.72	6.30
China's mainland	6198	3.77	6.36	4.84	30.18

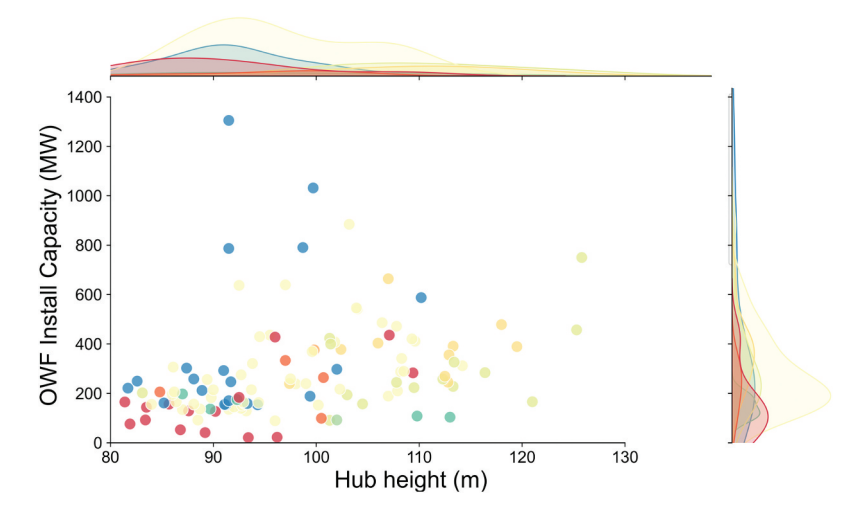


Figure 8. Distribution of hub heights and corresponding installed capacities of OWFs across various regions of China's mainland in 2022.

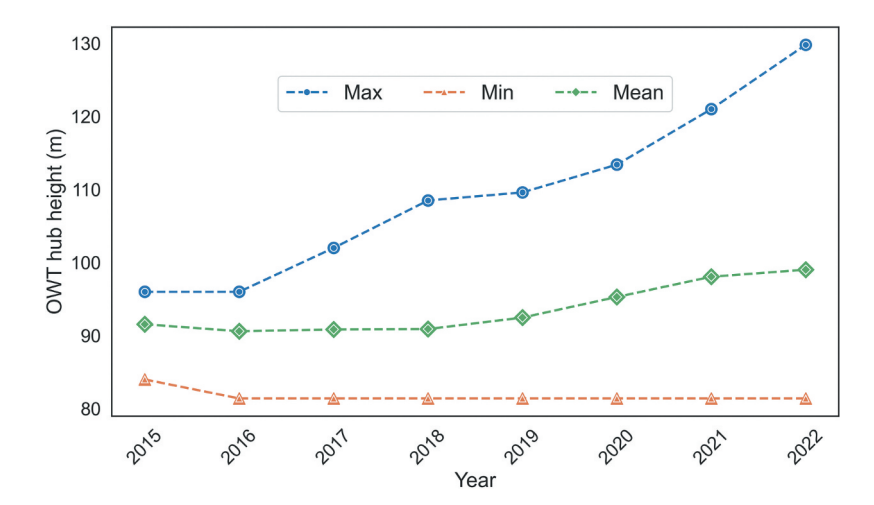


Figure 9. The hub height trends of OWTs in China's mainland from 2015 to 2022. The Y-axis of represents three statistical metrics for the hub heights of OWTs from 2015 to 2022: maximum, minimum, and average values for each year.

Table 3. Minimum, maximum, average, and total values of OWT and OWF count and installed capacity from 2015 to 2022.

	. , ,					
Year	OWT	Max (MW)	Min (MW)	Mean (MW)	OWF	All (GW)
2015	265	4.46	3.24	4	5	1.06
2016	456	4.46	3	3.89	13	1.77
2017	877	5.13	3	3.92	23	3.44
2018	1295	5.91	3	3.93	39	5.1
2019	1830	6.04	3	4.1	45	6.13
2020	3465	6.53	3	4.42	74	15.32
2021	5558	7.55	3	4.73	100	26.29
2022	6198	8.82	3	4.84	109	30.18

development scale. By the end of December from 2015 to 2022, the number of OWTs in China's mainland increased from 265 to 6,198, and the cumulative installed capacity increased from 1.06 GW to 30.18 GW, showing rapid growth. The annual growth rates of cumulative installed capacity for OWTs from 2019 to 2021 exceeded 70%. In 2021, the installed capacity reached 26.29 GW. This was four times the capacity in 2019, setting a new record for the total installed capacity of OWTs in China. However, the annual growth rate in 2022 was only 14.8%, closely related to the policy of subsidy cancellation for OWTs in China in 2022.

For the sake of the installed capacity per unit of OWTs, the maximum installed capacity per turbine tripled by twofold from 4.46 MW in 2015 to 8.82 MW in 2022, while the average installed capacity per turbine decreased slowly from 4 MW in 2015 to 3.89 MW in 2016, and then increased year by year to 4.84 MW in 2022. This trend is closely related to the national demand for clean energy production, OWT technology maturity, and supply chain improvements. The minimum installed capacity has remained unchanged since the completion of the Nanri Island OWF in Fujian in 2016, further indicating the trend of large-scale OWT installation. The application prospects of offshore wind power in China are promising under the "14th Five-Year Plan" and the dual carbon goals of "peak carbon emissions and carbon neutrality," with significant development potential in the future.

Regarding OWFs, the number of OWFs increased from 5 in 2015 to 109 in 2022, showing a year-on-year growth trend. The installed capacity of all OWFs in China's mainland from 2015 to 2022 and their corresponding unit heights are shown in Figure 10. The maximum installed capacity of OWFs increased from 632.89 MW in 2015 to 1,305.04 MW in 2022. OWFs with a capacity exceeding 100 MW raised from 2 in 2015 to 99 in 2022, accounting for 90.83% of the total number of OWFs in China's mainland in 2022. The hub heights of OWTs in China's mainland between 2015 and 2022 were mainly between 80 m and 110 m, while the installed capacity of OWFs ranged from 100 MW to 400 MW. This suggests that most of the OWTs currently operational in China's mainland have medium-scale hub heights and installed capacities. Policies such as the 14th Five-Year Plan will further promote the development of large-scale installed capacity OWT projects and the production of clean energy for carbon neutrality. Additionally, significant differences in the scale of installed capacity of OWTs among Chinese provinces from 2015 to 2022 are evident, as detailed in the supplementary material (Figure S2 and S3).

5. Discussion

5.1. Comparison with statistical reports

We compared and verified the cumulative-installed capacity values with the statistics released by the

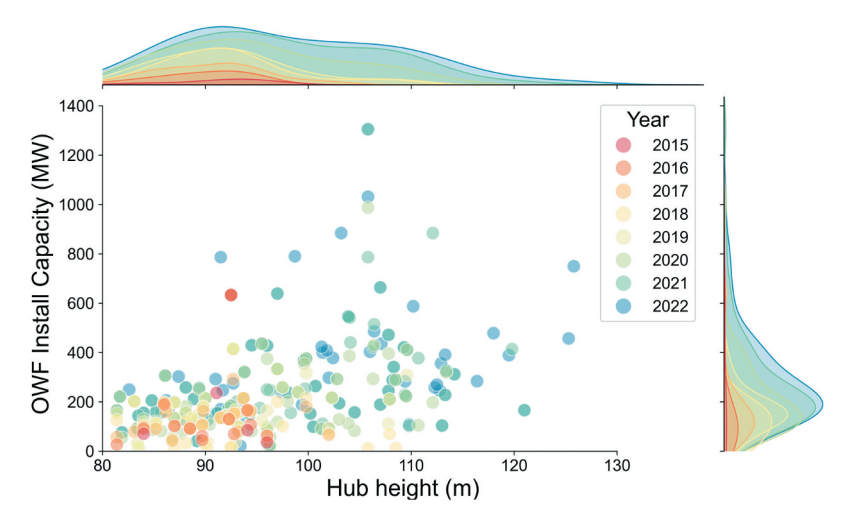


Figure 10. Installed capacity and hub height trends of OWFs in China's mainland from 2015 to 2022.

GWEC and CWEA for the years 2015-2022 (Figure 11). We calculated the ratios of our study's results to those of GWEC and CWEA. This study also estimated the individual installed capacities of OWTs and the installed capacities of OWFs from 2015 to 2022. These remote sensing-based estimates are highly consistent with GWEC and CWEA data for several years, particularly in 2015, 2018, 2019, 2021, and 2022. The accuracy for these years consistently approaches or exceeds 90%, with R^2 (R-squared) all at 0.99 and RMSE of 0.77 GW and 0.62 GW, respectively. In most years, the study results were more aligned with CWEA data. For instance, in 2016, the accuracy compared to CWEA data was 95.27%, while it was only 77.08% compared to GWEC data. Similar patterns were observed in 2017 and subsequent years. These official reports largely validate the credibility of the estimated installed capacity in this study and demonstrate that the combination of deep learning models and Sentinel-2 data can monitor offshore wind energy reserves. We analyzed Sentinel-2 and high-resolution imagery data for 2020, identifying over 3,000 OWTs with a cumulative installed capacity of approximately 15 GW. The CWEA reports 787 new OWTs in 2020, whereas remote sensing imagery indicates 1635 new OWTs, far exceeding CWEA's statistical results. The remote sensing estimate closely matches the 2020 OWT numbers reported in Hoeser, Feuerstein, and Kuenzer (2022). However, statistics from the GWEC and the CWEA indicate a lower cumulative installed capacity of around 10 GW for the same year. The discrepancy primarily stems from differences in statistical methodologies. Remote sensing-based estimates are derived directly from imagery data, allowing for real-time monitoring of OWTs. In comparison, the CWEA and GWEC statistics rely on reports submitted by local departments, which may have been delayed due to exceptional events like the COVID-19 pandemic. Furthermore, CWEA and GWEC reports offer only large-scale regional or national summaries, while this study can promptly provide individual OWT and OWF hub height and

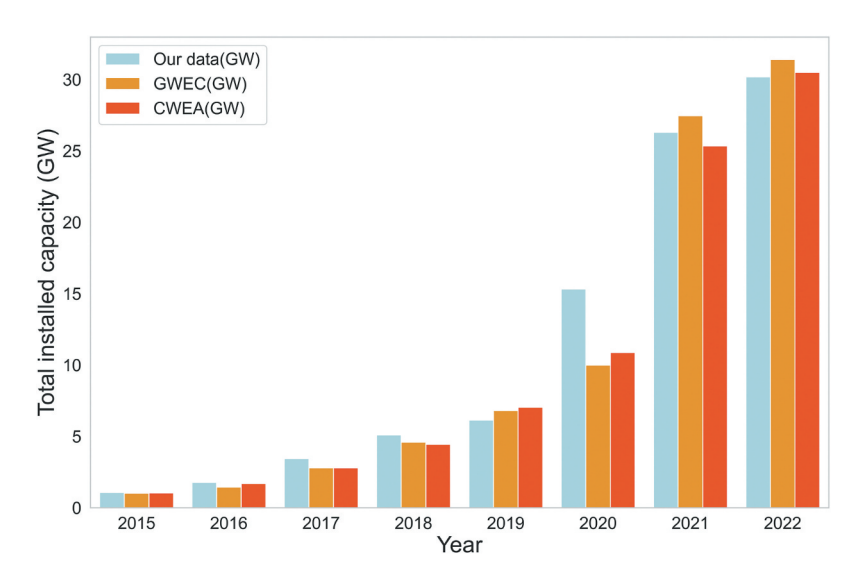


Figure 11. Comparison of the total installed capacity of OWTs from 2015 to 2022 between our data and that of GWEC and CWEA.



installed capacity information, providing flexibility in summarizing OWT and OWF attribute information. This provides valuable reference data for the sustainable development of offshore wind energy in China and contributes to achieving the "double carbon" goals.

5.2. Uncertainty analysis

The uncertainties in this study mainly originate from two aspects. First is the uncertainty in calculating the hub height of wind turbines in wind farms, primarily determined by the accuracy of shadow recognition. In this study, the median hub height of all turbines in a wind farm was used to represent the turbine height within that range. We randomly selected one OWF from each coastal province where OWTs were installed and conducted statistics on the hub heights of all OWTs in each OWF, calculating the mean, median, and standard deviation (Figure 12). The results show that the variance calculated for each OWF is less than 0.15, indicating that the hub heights are relatively consistent. Therefore, using the median to represent the hub height of a wind farm can effectively reduce errors. The second uncertainty arises from simulating the relationship between turbine hub height and installed capacity. In this study, polynomial curves, linear, exponential, and logarithmic fittings were conducted on the hub height and installed capacity of 60 OWFs, where the polynomial curve fitting with the highest R^2 was selected. However, the highest value was only 0.77, suggesting that increasing the number of measured samples in the future could make the optimization results more reliable (Shao and Liu 2024).

5.3. Offshore wind power development potential in China

Estimating the potential for large-scale offshore wind power development is crucial for achieving China's "double carbon" goals and for future planning of offshore wind energy projects. This study used the latest wind turbine models from Goldwind Science & Technology Co., Ltd., a leading company in the domestic wind power market, to estimate the potential power generation capacity (Liu et al. 2022). Based on regional differences in multi-year average wind speeds and the average hub height of OWTs in China, three types of OWTs with a hub height of 100 m were selected for different sea regions. The actual power output is calculated by multiplying the theoretical power output by the capacity factor (CF). The actual integrated loss factor ranges between 70% and 80%, meaning the CF usually varies from 20% to 30% (Liu et al. 2020; Wang et al. 2022; Zhu 2019), with an average value of 25%. This study estimates the annual energy production (AEP) for

China's offshore wind power by considering the rated capacity of different types of OWTs. Given the actual area of OWFs, policy factors, and the potential reduction in power generation due to turbulent wake effects caused by overly dense OWT spacing, the horizontal spacing between OWTs was set at 10D and the vertical spacing at 5D, where D represents the rotor diameter (Lundquist et al. 2019).

This study estimates that the technical potential for offshore wind energy resources within a 150km range from the coast of China, at a height of 100 m, is 3,759.51 GW, with an annual energy production of approximately 7,952.43 TWh, assuming no consideration of development costs, transmission losses, or marine protected areas (Table 4). At the provincial level, Guangdong has the largest potential for offshore wind power development, with an estimated capacity of 811.19 GW and a projected annual energy production of 1,776.52 TWh. This is followed by Taiwan, Zhejiang, Fujian, Shandong, and Hainan, all with capacities exceeding 300 GW. Provinces such as Hebei, Shanghai, Tianjin, and Liaoning have less than 100 GW capacities. At the national level, China's offshore wind power installed capacity is expected to exceed 88 GW by 2030, achieving a peak in carbon emissions. The potential capacity of OWTs in China far exceeds the installed capacity required to meet carbon neutrality goals, with the potential to meet 9.2% of China's national electricity demand in 2022 (86,372 TWh). As of the end of 2022, China's offshore wind power installed capacity was less than 1% of its estimated technical potential. The development of offshore wind energy resources is significantly influenced by water depth. Based on the depth criteria (nearshore: 5-50 m; deep-sea: 50-100 m), the technical potential for wind energy resources at a 100-m height in nearshore China is approximately 1,997.79 GW, while the technical potential for deep-sea wind energy resources is about 1,761.72 GW. Concerning nearshore wind power development capacity, Jiangsu has the greatest potential, reaching 274.69 GW, followed by Guangdong, Shandong, Fujian, and Zhejiang, each with a nearshore wind energy technical potential exceeding 100 GW. Guangdong and Taiwan exhibit the highest potential for deep-sea wind power development, with Zhejiang, Hainan, and Fujian following. The development of these resources necessitates the use of floating platforms, a technology that is still in its nascent stages.

5.4. Limitations and future works

This study introduces a novel approach for estimating offshore wind turbine (OWT) installed capacity using Sentinel-2 imagery and deep learning techniques. To

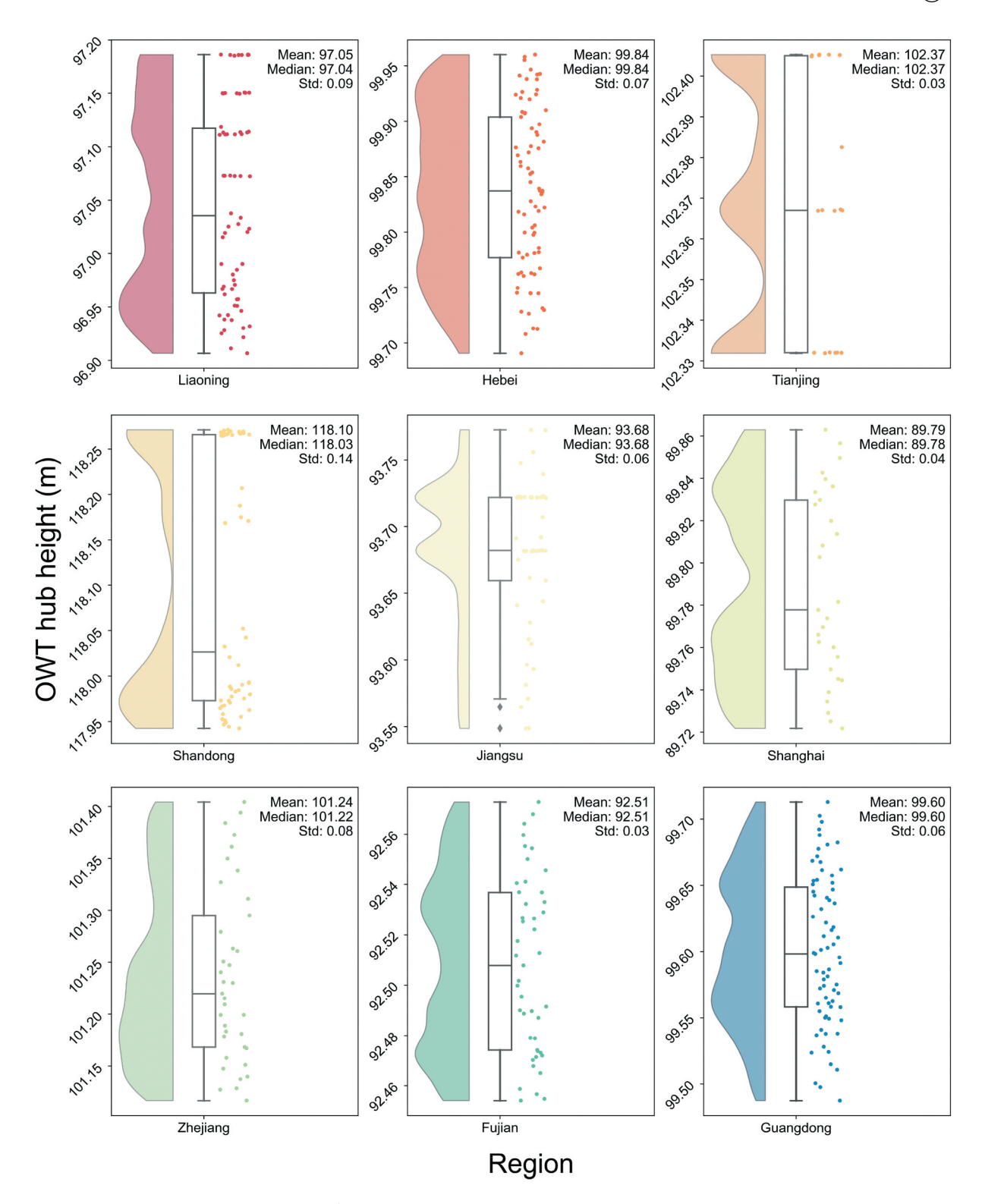


Figure 12. One OWF randomly selected from Liaoning, Hebei, Tianjin, Shandong, Jiangsu, Shanghai, Zhejiang, Fujian, and Guangdong provinces in 2022, where the hub heights of each OWT were recorded and the mean, median, and standard deviation were calculated.

address the limitations of traditional methods, a shadow extraction model was developed to derive OWT hub heights and establish a relationship between hub height and installed capacity. In the imagery, shadows indicate that OWT hubs often exhibit similar brightness to clear waterbodies, darker ground objects, and OWT blades. This similarity can result in challenges, such as inaccurate edge delineation,

waterbodies containing shadow information, and shadows containing blade artifacts. Further research is needed to validate the method and resolve these issues. Additionally, the complexity of shadow formation and image quality poses further challenges. Addressing these interferences is essential for achieving high-precision extraction of OWT hub shadows. The future development of OWTs will likely focus on large single-

Table 4. Wind turbine types, parameters	applicable area standards	. and annual electricity	generation in different regions.

Region	Wind turbine type	Rotor diameter (m)	Installed capacity (MW)	Area (km²)	Theoretical number of turbines	Installed capacity (GW)	Generation (TWh)
Liaoning	GW 175-6	175	6	43208.47	21377	128.26	280.90
Tianjin	GW 175-6	175	6	1529.50	757	4.54	9.94
Hebei	GW 175-6	175	6	20265.92	10026	60.16	131.75
Shandong	GW 175-6	175	6	114712.76	56753	340.52	745.74
Jiangsu	GW 175-6	175	6	100947.23	49943	299.66	656.25
Shanghai	GW 175-6	175	6	17206.91	8513	51.08	111.86
Zhejiang	GW 175-8	175	8	144920.45	71698	573.59	1256.16
Fujian	GW 154-6.7	154	7	110506.63	70600	473.02	1035.91
Guangdong	GW 175-8	175	8	204953.47	101399	811.19	1776.52
Guangxi	GW 175-8	175	8	26383.93	13053	104.43	228.69
Hainan	GW 175-8	175	8	76857.55	38025	304.20	666.19
Taiwan	GW 154-6.7	154	7	142243.82	90876	608.87	1333.42
All				1003736.65	533021	3759.51	7952.43

unit capacities, floating OWTs, and combining wind energy with wave and tidal energy, which will require significant innovation. Other critical considerations include the impact of precipitation and extreme weather on OWT blade erosion (Mishnaevsky et al. 2021; Pugh and Stack 2021), the storage and conversion of high-power offshore wind energy (Catalán et al. 2023; Zeng et al. 2024), and the maintenance and management of OWFs (Márquez and Papaelias 2020; Peinado Gonzalo et al. 2022). To address these challenges and seize emerging opportunities, China must accelerate research into floating OWTs and explore the integration of offshore wind energy with wave and tidal energy. This strategy will support the sustainable development of offshore wind power and enhance ocean energy efficiency.

6. Conclusions

The increasing demand for renewable energy and carbon reduction initiatives has heightened the importance of calculating attributes like the installed capacity of OWTs. This study developed a deep learning model called VC-Unet, which combines a backbone network and an attention mechanism in parallel. The VC-Unet model is designed to extract OWT hub shadows from Sentinel-2 imagery, enabling the calculation of shadow length and subsequently determining OWT hub height and installed capacity. The proposed model achieves an IoU of 98.96 ± 0.05, a mPA of 99.66 \pm 0.03, a precision of 99.58 \pm 0.01, a recall of 99.38 \pm 0.06, and an F1-score of 99.48 \pm 0.02, demonstrating excellent performance in distinguishing between waterbodies and OWT hub shadows.

From 2015 to 2022, the cumulative installed capacity of offshore wind power in China's mainland grew from 1.06 GW (265 OWTs, 5 OWFs) to 30.18 GW (6,198 OWTs, 109 OWFs), marking a 28-fold increase in total installed capacity over 8 years. The growth rate peaked at 149.92% in 2020 but slightly declined to 14.8% in 2022. During this period, the average hub height per turbine rose from 91.55 m to 99.02 m, while the average installed capacity per turbine increased from 4 MW to 4.84 MW. The maximum installed capacity of OWFs increased from 632.89 MW in 2015 to 1,305.04 MW in 2022 (geographically), indicating a trend toward the large-scale development of both OWTs and OWFs. As of the end of 2022, the maximum hub height of OWTs reached 129.8 m, and OWFs with a capacity greater than 100 MW accounted for 90.83% of the total OWF capacity in China's mainland.

Additionally, this study demonstrated accuracy and robustness through error analysis compared to other data sources, validating the model's application in China's mainland. OWTs in China's mainland are mainly deployed in nearshore areas, suggesting significant potential for development in deeper offshore areas. In the future, leveraging floating wind farm technology and wind power integration techniques to move toward high-power, deep offshore areas could be considered. Increasing hub heights to harness more wind energy could contribute to the sustainable development of wind energy.

Disclosure statement

No potential conflict of interest was reported by the author(s).

Funding

This work was supported by the Open Research Fund of the State Key Laboratory of Estuarine and Coastal Research [Grant No. SKLEC-KF202307].

Notes on contributors

Qiannan Ding is currently a Ph.D. student in physical geography at the State Key Laboratory of Estuarine and Coastal Research (SKLEC), East China Normal University. Her research interests include coastal time series remote sensing and deep learning.



Chunpeng Chen received his PhD degree from East China Normal Univsersity and is currently a postdoctoral fellow in the Hong Kong Polytechnic University. His research interests include coastal remote sensing and deep learning.

Bo Tian is currently an associate professor at the SKLEC, East China Normal University. His research interests include coastal zone assessment and remote sensing, as well as GIS development and application.

Wenxiang Ji is a master's student at East China Normal University. He specializes in coastal zone remote sensing, geographic information systems (GIS), and UAV-based observation.

Bin Zhang is currently pursuing master degree at East China Normal University. His research interests include multisource remote sensing and machine learning.

Xue Li is currently pursuing a master degree at East China Normal University, with research interests in coastal remote sensing and deep learning.

Qing Yuan is currently an engineer at East China Normal University. His research interests are GIS Development and Data Analysis.

ORCID

Qiannan Ding (b) http://orcid.org/0009-0008-9362-1813 Chunpeng Chen http://orcid.org/0009-0007-7649-2178 Bo Tian (b) http://orcid.org/0000-0003-1323-7878 Wenxiang Ji http://orcid.org/0009-0001-4160-1721 Bin Zhang http://orcid.org/0009-0008-5317-3075 Xue Li http://orcid.org/0009-0004-2452-0403 Qing Yuan http://orcid.org/0009-0008-8716-8207

Data availability statement

All data that support the findings of this study are included in this manuscript and its supplementary information files.

References

- Aghdami-Nia, M., R. Shah-Hosseini, A. Rostami, and S. Homayouni. 2022. "Automatic Coastline Extraction Through Enhanced Sea-Land Segmentation by Modifying Standard U-Net." International Journal of Applied Earth Observation and Geoinformation 109:102785. https://doi.org/10.1016/j.jag.2022.102785.
- Badger, M., A. Peña, A. N. Hahmann, A. A. Mouche, and C. B. Hasager. 2016. "Extrapolating Satellite Winds to Turbine Operating Heights." Journal of Applied Meteorology & Climatology 55 (4): 975-991. https://doi. org/10.1175/JAMC-D-15-0197.1.
- Bai, T., L. Wang, D. Yin, K. Sun, Y. Chen, W. Li, and D. Li. 2023. "Deep Learning for Change Detection in Remote Sensing: A Review." Geo-Spatial Information Science 26 (3): 262-288. https://doi.org/10.1080/10095020.2022. 2085633.
- Beaumont, N. J., M. Aanesen, M. C. Austen, T. Börger, J. R. Clark, M. Cole, T. Hooper, P. K. Lindeque, C. Pascoe, and K. J. Wyles. 2019. "Global Ecological, Social and Economic Impacts of Marine Plastic." Marine Pollution Bulletin 142:189-195. https://doi.org/ 10.1016/j.marpolbul.2019.03.022.

- Benali Amjoud, A., and M. Amrouch. 2020. "Convolutional Neural Networks Backbones for Object Detection." In Image and Signal Processing, edited by A. E. Moataz, D. Mammass, A. Mansouri, and F. Nouboud, 282-289. Lecture Notes in Computer Science. Cham: Springer International Publishing. https://doi.org/10.1007/978-3-030-51935-3_30.
- Cao, Y., and X. Huang. 2021. "A Deep Learning Method for Building Height Estimation Using High-Resolution Multi-View Imagery Over Urban Areas: A Case Study of 42 Chinese Cities." Remote Sensing of Environment 264:112590. https://doi.org/10.1016/j.rse.2021.112590.
- Catalán, P., Y. Wang, J. Arza, and Z. Chen. 2023. "A Comprehensive Overview of Power Converter Applied in High-Power Wind Turbine: Key Challenges and Potential Solutions." IEEE Transactions on Power Electronics 38 (5): 6169-6195. https://doi.org/10.1109/ TPEL.2023.3234221.
- Chen, C., C. Zhang, B. Tian, W. Wu, and Y. Zhou. 2023a. "Tide2Topo: A New Method for Mapping Intertidal Topography Accurately in Complex Estuaries and Bays with Time-Series Sentinel-2 Images." ISPRS Journal of Photogrammetry & Remote Sensing 200:55-72. https:// doi.org/10.1016/j.isprsjprs.2023.05.004.
- Chen, C., C. Zhang, B. Tian, W. Wu, and Y. Zhou. 2023b. "Mapping Intertidal Topographic Changes in a Highly Turbid Estuary Using Dense Sentinel-2 Time Series with Deep Learning." Isprs Journal of Photogrammetry & Remote Sensing 205:1-16. https://doi.org/10.1016/j. isprsjprs.2023.09.022.
- Ciocarlan, A., and A. Stoian. 2021. "Ship Detection in Sentinel 2 Multi-Spectral Images with Self-Supervised Learning." Remote Sensing 13 (21): 4255. https://doi.org/ 10.3390/rs13214255.
- Du, Z., Z. Liu, Q. Zhou, Y. Zhao, Z. Sun, and L. Li. 2024. "Research on Process Safety of Offshore Wind Turbines Installation: A Theoretical Model and Empirical Evidence." Process Safety and Environmental Protection 181:493-501. https://doi.org/10.1016/j.psep.2023.11.062.
- Duan, H. 2017. "Emissions and Temperature Benefits: The Role of Wind Power in China." Environmental Research 152:342-350. https://doi.org/10.1016/j.envres.2016.07.016.
- Dunnett, S., A. Sorichetta, G. Taylor, and F. Eigenbrod. 2020. "Harmonised Global Datasets of Wind and Solar Farm Locations and Power." Scientific Data 7 (1): 130. https://doi.org/10.1038/s41597-020-0469-8.
- Fan, J., Y. Ma, T. Liang, and G. Cui. 2024. "Multi-Source Remote Sensing Big Data Mining Reveals Cross-Regional Correlation Between Aquaculture and Enteromorpha Disaster Outbreaks." Geo-Spatial Information Science: 1-13. https://doi.org/10.1080/10095020.2023.2282672.
- Feng, Y., H. Lin, S. L. Ho, J. Yan, J. Dong, S. Fang, and Y. Huang. 2015. "Overview of Wind Power Generation in China: Status and Development." Renewable and Sustainable Energy Reviews 50:847-858. https://doi.org/ 10.1016/j.rser.2015.05.005.
- Frantz, D., F. Schug, A. Okujeni, C. Navacchi, W. Wagner, S. van der Linden, and P. Hostert. 2021. "National-Scale Mapping of Building Height Using Sentinel-1 and Sentinel-2 Time Series." Remote Sensing of Environment 252:112128. https://doi.org/10.1016/j.rse.2020.112128.
- Global Wind Energy Council. 2023. Global Wind Report 2023. https://gwec.net/global-wind-report-2022/.
- Gong, P., Z. Li, H. Huang, G. Sun, and L. Wang. 2011. "ICESat GLAS Data for Urban Environment Monitoring." IEEE Transactions on Geoscience &

- Remote Sensing 49 (3): 1158-1172. https://doi.org/10. 1109/TGRS.2010.2070514.
- Gong, W., C. Huang, F. Zhao, and J. Lu. 2025. "Estimation of Annual Harvested Wood Products Based on Remote Sensing and TPO Survey Data." Geo-Spatial Information Science 28 (1): 36-48. https://doi.org/10.1080/10095020. 2024.2313329.
- Greidanus, H., M. Alvarez, C. Santamaria, F.-X. Thoorens, N. Kourti, and P. Argentieri. 2017. "The SUMO Ship Detector Algorithm for Satellite Radar Images." Remote Sensing 9 (3): 246. https://doi.org/10.3390/rs9030246.
- Han, X., X. Li, J. Yang, W. Tao, G. Han, J. Wang, Y. Wang, Q. Bao, L. Chen, and W. Li. 2025. "Evaluation and Deep Learning-Based Calibration of Nearshore Sea Surface Wind Speeds from FY-3E GNOS-II and TIANMU $Missions." \ \textit{Geo-Spatial Information Science:} \ 1-12.$ https://doi.org/10.1080/10095020.2024.2441473.
- He, H., D. Yang, S. Wang, S. Wang, and Y. Li. 2019. "Road Extraction by Using Atrous Spatial Pyramid Pooling Integrated Encoder-Decoder Network and Structural Similarity Loss." Remote Sensing 11 (9): 1015. https:// doi.org/10.3390/rs11091015.
- He, K., X. Zhang, S. Ren, and J. Sun. 2016. "Deep Residual Learning for Image Recognition." In 2016 IEEE Conference on Computer Vision and Pattern Recognition (CVPR), 770–778. https://doi.org/10.1109/CVPR.2016.90.
- Hoeser, T., S. Feuerstein, and C. Kuenzer. 2022. "DeepOWT: A Global Offshore Wind Turbine Data Set Derived with Deep Learning from Sentinel-1 Data." Earth System Science Data 14 (9): 4251-4270. https://doi.org/ 10.5194/essd-14-4251-2022.
- Hoeser, T., and C. Kuenzer. 2022. "Global Dynamics of the Offshore Wind Energy Sector Monitored with Sentinel-1: Turbine Count, Installed Capacity and Specifications." International Journal of Applied Earth Observation and Geoinformation 112:102957. https:// doi.org/10.1016/j.jag.2022.102957.
- Hu, Y., and Q. Zhang. 2018. "The Extraction of Building Shadow and the Estimation of Building Heights Based on Morphology and Spectral Characteristic Parameters." Bulletin of Surveying and Mapping 6:22–26. https://doi. org/10.13474/j.cnki.11-2246.2018.0170.
- Huang, H., P. Chen, X. Xu, C. Liu, J. Wang, C. Liu, N. Clinton, and P. Gong. 2022. "Estimating Building Height in China from ALOS AW3D30." Isprs Journal of Photogrammetry & Remote Sensing 185:146-157. https:// doi.org/10.1016/j.isprsjprs.2022.01.022.
- Huang, X., and L. Zhang. 2012. "Morphological Building/ Shadow Index for Building Extraction from High-Resolution Imagery Over Urban Areas." IEEE Journal of Selected Topics in Applied Earth Observations & Remote Sensing 5 (1): 161–172. https://doi.org/10.1109/ JSTARS.2011.2168195.
- Kikaki, K., I. Kakogeorgiou, I. Hoteit, and K. Karantzalos. 2024. "Detecting Marine Pollutants and Sea Surface Features with Deep Learning in Sentinel-2 Imagery." Isprs Journal of Photogrammetry & Remote Sensing 210:39–54. https://doi.org/10.1016/j.isprsjprs.2024.02. 017.
- Lee, J.-Y., and S.-H. Hong. 2024. "Construction of Digital Elevation Models on the Intertidal Flats Using TanDEM-X Bistatic Observations." IEEE Geoscience & Remote Sensing Letters 21:1-5. https://doi.org/10.1109/ LGRS.2024.3370258.
- Liang, X., H. Qi, X. Deng, J. Chen, S. Cai, Q. Zhang, Y. Wang, A. Kukko, and J. Hyyppä. 2025. "ForestSemantic: A Dataset for Semantic Learning of

- Forest from Close-Range Sensing." Geo-Spatial Information Science 28 (1): 185-211. https://doi.org/10. 1080/10095020.2024.2313325.
- Liu, L., Y. Wang, Z. Wang, S. Li, J. Li, G. He, Y. Li, et al. 2022. "Potential Contributions of Wind and Solar Power to China's Carbon Neutrality." Resources, Conservation & Recycling 180:106155. https://doi.org/10.1016/j.resconrec. 2022.106155.
- Liu, L., Z. Wang, Y. Wang, J. Wang, R. Chang, G. He, W. Tang, et al. 2020. "Optimizing Wind/Solar Combinations at Finer Scales to Mitigate Renewable Energy Variability in China." Renewable and Sustainable Energy Reviews 132:110151. https://doi.org/ 10.1016/j.rser.2020.110151.
- Liu, R., H. Zhang, K. H. A. Yip, J. Ling, Y. Lin, and H. Huang. 2023. "Automatic Building Height Correction Estimation with Shadow Heterogeneous Compact Cities Using Stereo Gaofen-7 Data at Sub-Meter Resolution." Journal of Building Engineering 69:106283. https://doi.org/10.1016/j.jobe. 2023.106283.
- Lundquist, J. K., K. K. DuVivier, D. Kaffine, and J. M. Tomaszewski. 2019. "Costs and Consequences of Wind Turbine Wake Effects Arising from Uncoordinated Wind Energy Development." Nature Energy 4:26. https:// doi.org/10.1038/s41560-018-0281-2.
- Magruder, L., A. Neuenschwander, and B. Klotz. 2021. "Digital Terrain Model Elevation Corrections Using Space-Based Imagery and ICESat-2 Laser Altimetry." Remote Sensing of Environment 264:112621. https://doi. org/10.1016/j.rse.2021.112621.
- Majidi Nezhad, M., M. Neshat, G. Piras, and D. Astiaso Garcia. 2022. "Sites Exploring Prioritisation of Offshore Wind Energy Potential and Mapping for Wind Farms Installation: Iranian Islands Case Studies." Renewable and Sustainable Energy Reviews 168:112791. https://doi. org/10.1016/j.rser.2022.112791.
- Mandroux, N., T. Dagobert, S. Drouyer, and R. G. Von Gioi. 2021. "Wind Turbine Detection on Sentinel-2 Images." In 2021 IEEE International Geoscience and Remote Sensing Symposium IGARSS, 4888–4891. https://doi.org/10.1109/ IGARSS47720.2021.9554578.
- Márquez, F. P. G., and M. Papaelias. 2020. "Chapter 3 an Overview of Wind Turbine Maintenance Management." In Non-Destructive Testing and Condition Monitoring Techniques for Renewable Energy Industrial Assets, edited by M. Papaelias, F. P. G. Márquez, and A. Karyotakis, 31–47. Boston: Butterworth-Heinemann. https://doi.org/ 10.1016/B978-0-08-101094-5.00003-4.
- Medina-Lopez, E., D. McMillan, J. Lazic, E. Hart, S. Zen, A. Angeloudis, E. Bannon, et al. 2021. "Satellite Data for the Offshore Renewable Energy Sector: Synergies and Innovation Opportunities." Remote Sensing Environment 264:112588. https://doi.org/10.1016/j.rse. 2021.112588.
- Mishnaevsky, L., C. B. Hasager, C. Bak, A.-M. Tilg, J. I. Bech, S. Doagou Rad, and S. Fæster. 2021. "Leading Edge Erosion of Wind Turbine Blades: Understanding, and Protection." Renewable Energy Prevention 169:953-969. https://doi.org/10.1016/j.renene.2021.01.044.
- Moubayed, F., R. Becker, and J. Blankenbach. 2025. "Geodata-Based Number of Floor Estimation for Urban Residential Buildings as an Input Parameter for Energy Modelling." Geo-Spatial Information Science: 1-27. https://doi.org/10.1080/10095020.2025.2465307.
- Pazheri, F. R., M. F. Othman, and N. H. Malik. 2014. "A Review on Global Renewable Electricity Scenario."



- Renewable and Sustainable Energy Reviews 31:835-845. https://doi.org/10.1016/j.rser.2013.12.020.
- Peinado Gonzalo, A., T. Benmessaoud, M. Entezami, and F. P. García Márquez. 2022. "Optimal Maintenance Management of Offshore Wind Turbines by Minimizing the Costs." Sustainable Energy Technologies and Assessments 52:102230. https://doi.org/10.1016/j. seta.2022.102230.
- Pepe, M., D. Costantino, V. S. Alfio, G. Vozza, and E. Cartellino. 2021. "A Novel Method Based on Deep Learning, GIS and Geomatics Software for Building a 3D City Model from VHR Satellite Stereo Imagery. ISPRS International Journal of Geo-Information 10 (10): 697. https://doi.org/10.3390/ijgi10100697.
- Pugh, K., and M. M. Stack. 2021. "Rain Erosion Maps for Wind Turbines Based on Geographical Locations: A Case Study in Ireland and Britain." Journal of Bio- and Tribo-Corrosion 7 (1): 34. https://doi.org/10.1007/s40735-021-00472-0.
- Rand, J. T., L. A. Kramer, C. P. Garrity, B. D. Hoen, J. E. Diffendorfer, H. E. Hunt, and M. Spears. 2020. "A Continuously Updated, Geospatially Rectified Database of Utility-Scale Wind Turbines in the United States." Scientific Data 7 (1): 15. https://doi.org/10.1038/ s41597-020-0353-6.
- Redmon, J., and A. Farhadi. 2017. "YOLO9000: Better, Faster, Stronger." In 2017 IEEE Conference on Computer Vision and Pattern Recognition (CVPR), 6517-6525. Honolulu, HI: IEEE. https://doi.org/10.1109/CVPR.
- Ronneberger, O., P. Fischer, and T. Brox. 2015. "U-Net: Convolutional Networks for Biomedical Image Segmentation." In Medical Image Computing and Computer-Assisted Intervention - MICCAI 2015, edited by N. Navab, J. Hornegger, W. M. Wells, and A. F. Frangi, 234-241. Lecture Notes in Computer Science. Cham: Springer International Publishing. https://doi.org/10. $1007/978-3-319-24574-4_28.$
- Shao, Y., and J. Liu. 2024. "Uncertainty Quantification for Dynamic Responses of Offshore Wind Turbine Based on Manifold Learning." Renewable Energy 222:119798. https://doi.org/10.1016/j.renene.2023.119798.
- Simonyan, K., and A. Zisserman. 2015. "Very Deep Convolutional Networks for Large-Scale Image Recognition." arXiv. https://doi.org/10.48550/arXiv. 1409.1556.
- Sun, G., H. Huang, Q. Weng, A. Zhang, X. Jia, J. Ren, L. Sun, and X. Chen. 2019. "Combinational Shadow Index for Building Shadow Extraction in Urban Areas from Sentinel-2A MSI Imagery." International Journal of Applied Earth Observation and Geoinformation 78:53-65. https://doi.org/10.1016/j.jag.2019.01.012.
- Sun, Y., Y. Hua, L. Mou, and X. X. Zhu. 2019. "Large-Scale Building Height Estimation from Single VHR SAR Image Using Fully Convolutional Network and GIS Building Footprints." 2019 Joint Urban Remote Sensing Event (JURSE): 1-4. https://doi.org/10.1109/JURSE.2019. 8809037.
- Sun, Y., L. Mou, Y. Wang, S. Montazeri, and X. X. Zhu. 2022. "Large-Scale Building Height Retrieval from Single SAR Imagery Based on Bounding Box Regression Networks." Isprs Journal of Photogrammetry & Remote Sensing 184:79-95. https://doi.org/10.1016/j.isprsjprs. 2021.11.024.
- Szegedy, C., W. Liu, Y. Jia, P. Sermanet, S. Reed, D. Anguelov, D. Erhan, V. Vanhoucke, and "Going Rabinovich. 2015. Deeper

- Convolutions." In 2015 IEEE Conference on Computer Vision and Pattern Recognition (CVPR), 1-9. https://doi. org/10.1109/CVPR.2015.7298594.
- Wang, J., X. Hu, Q. Meng, L. Zhang, C. Wang, X. Liu, and M. Zhao. 2021. "Developing a Method to Extract Building 3D Information from GF-7 Data." Remote Sensing 13 (22): 4532. https://doi.org/10.3390/rs13224532.
- Wang, K., W. Xiao, T. He, and M. Zhang. 2024. "Remote Sensing Unveils the Explosive Growth of Global Offshore Wind Turbines." Renewable and Sustainable Energy Reviews 191:114186. https://doi.org/10.1016/j.rser.2023. 114186.
- Wang, M., P. Ullrich, and D. Millstein. 2018. "Datasets on Hub-Height Wind Speed Comparisons for Wind Farms in California." Data in Brief 19:214-221. https://doi.org/ 10.1016/j.dib.2018.05.031.
- Wang, R., G. Li, Y. Lu, and D. Lu. 2024. "A Comparative Analysis of Grid-Based and Object-Based Modeling Approaches for Poplar Forest Growing Stock Volume Estimation in Plain Regions Using Airborne LiDAR Data." Geo-Spatial Information Science 27 (5): 1441–1459. https://doi.org/10.1080/10095020.2023. 2169199.
- Wang, Y., Q. Chao, L. Zhao, and R. Chang. 2022. "Assessment of Wind and Photovoltaic Power Potential in China." Carbon Neutrality 1 (1): 15. https://doi.org/10. 1007/s43979-022-00020-w.
- Wass, R. 2018. Design of Wind Turbine Tower Height and Blade Length: An Optimization Approach. Fayetteville, AR: University of Arkansas. https://scholarworks.uark. edu/meeguht/70.
- Woo, S., J. Park, J. Y. Lee, and I. S. Kweon. 2018. "CBAM: Convolutional Block Attention Module." arXiv. https:// doi.org/10.48550/arXiv.1807.06521.
- Xu, W., Y. Liu, W. Wu, Y. Dong, W. Lu, Y. Liu, B. Zhao, H. Li, and R. Yang. 2020. "Proliferation of Offshore Wind Farms in the North Sea and Surrounding Waters Revealed by Satellite Image Time Series." Renewable and Sustainable Energy Reviews 133:110167. https://doi.org/ 10.1016/j.rser.2020.110167.
- Yi, Y. 2018. "China Offshore Wind Power 2018." Electric Power Equipment Management 12:81-83.
- Zeng, T., X. Cao, H. Wang, and W. Zhao. 2024. "Research on Control Strategy of Large Offshore Wind Power Generation System." In The Proceedings of the 18th Annual Conference of China Electrotechnical Society, edited by Q. Yang, Z. Li, and A. Luo, 624-632. Singapore: Springer Nature. https://doi. org/10.1007/978-981-97-1351-6_66.
- Zhang, M., D. Li, G. Li, and D. Lu. 2024. "Vegetation Classification in a Subtropical Region with Sentinel-2 Time Series Data and Deep Learning." Geo-Spatial Information Science: 1-19. https://doi.org/10.1080/ 10095020.2024.2336604.
- Zhang, T., B. Tian, D. Sengupta, L. Zhang, and Y. Si. 2021. "Global Offshore Wind Turbine Dataset." Scientific Data 8 (1): 191. https://doi.org/10.1038/s41597-021-00982-z.
- Zhu, Q. Z. 2019. "Invesitigation on the Power Reduction Factor of Wind Farms." Wind Energy Industry 10.
- Zhu, X. X., and R. Bamler. 2010. "Very High Resolution Spaceborne SAR Tomography in Urban Environment." IEEE Transactions on Geoscience & Remote Sensing 48 (12): 4296-4308. https://doi.org/10.1109/TGRS.2010. 2050487.
- Zhuang, F., Z. Qi, K. Duan, D. Xi, Y. Zhu, H. Zhu, H. Xiong, and Q. He. 2020. "A Comprehensive Survey on Transfer Learning." arXiv. https://doi.org/10.48550/arXiv.1911. 02685.